Edge-enhanced negative magnetoresistance in a WSe_2/Fe_3GeTe_2 heterostructure

Xin Liao,[1] Zhen-Cun Pan,[1] Chun-Guang Chu,[1] Tong-Yang Zhao,[1] An-Qi Wang,[1,*] and Zhi-Min Liao[1,2,†]

[1]*State Key Laboratory for Mesoscopic Physics and Frontiers Science Center for Nano-optoelectronics, School of Physics, Peking University, Beijing 100871, China*

[2]*Hefei National Laboratory, Hefei 230088, China*

(Received 20 February 2023; revised 1 September 2023; accepted 18 September 2023; published 16 October 2023)

Dzyaloshinskii-Moriya interaction (DMI), the antisymmetric exchange interaction in noncentrosymmetric magnets, is a key ingredient in forming and manipulating the magnetic skyrmion, a promising candidate for next-generation data storage. With the development of non-Hermitian topological phases, the role of DMI has been extended to a broader stage recently. The non-Hermitian skin effect (NHSE) of magnons has been theoretically predicted to take place in magnetic systems with DMI and dissipation. Though exceptional band structures in van der Waals (vdW) magnetic structures have been observed, the NHSE of magnons has not been identified yet. Here we fabricate WSe_2/Fe_3GeTe_2 vdW heterostructure and observe the edge-enhanced negative magnetoresistance (NMR). The larger NMR at the sample's edges is attributed to the stronger electron-magnon scattering at the boundaries, indicating the edge accumulation of magnons. The aggregation of magnons towards sample boundaries is consistent with the magnonic NHSE, which is favored by the interface DMI and magnetic dissipation inherently in the heterojunction. Our work should be valuable for understanding the non-Hermitian topology in magnetic systems.

DOI: 10.1103/PhysRevB.108.144416

I. INTRODUCTION

Magnetic interaction in solid-state materials is crucial for fine design and broad application in spintronics. Dzyaloshinskii-Moriya interaction (DMI), the result of superexchange interaction and spin-orbit coupling (SOC), describes the antisymmetric magnetic interaction in the form of $E_{\mathrm{DM}} = \boldsymbol{D}_{ij} \cdot (\boldsymbol{S}_i \times \boldsymbol{S}_j)$, where $\boldsymbol{D}_{ij}$ is the DM vector and $\boldsymbol{S}_i$ and $\boldsymbol{S}_j$ are the electron spins [1,2]. This interaction exists in a system that lacks inversion symmetry and has strong SOC, driving adjacent spins tending to align perpendicular to each other, causing a noncollinear canted spin texture. DMI is believed to be a crucial element in the creation, annihilation, and manipulation of magnetic skyrmions and chiral domain walls, and has been observed in thin-film multilayer magnetic nanostructures [3–7], in graphene-ferromagnet interface [8], and transition metal dichalcogenide (TMDC)–ferromagnet van der Waals (vdW) heterostructure [9]. Due to their nanometer size [6] and robust current-driven dynamics at room temperature [3–5], magnetic skyrmions are promising for ultraintegrated and low-consumption information storage [10–12].

In recent years, the role of DMI in magnetic systems has been extended to the non-Hermitian regime, where exotic exceptional topological quantum states emerge beyond the conventional Hermitian quantum mechanics paradigm [13–18]. The magnon is the bosonic collective excitation of spin waves, with its quasiparticle number not generally conserved. Interactions of magnons could lead to an effective non-Hermitian Hamiltonian in an open dissipative magnetic system [19–22], providing a playground for exploring non-Hermitian topology. As a typical feature of non-Hermitian dynamics, exceptional structures (points, surfaces) have been observed in magnonic devices with magnon losses [23], and in microwave cavity magnon polaritons with dissipations [24,25]. Flebus *et al.* recently proposed that the non-Hermitian skin effect (NHSE) of magnons can be achieved when both magnetic dissipation and DMI are present [18]. Previous works have demonstrated that interfacial DMI in vdW magnets could be generated by strong Rashba SOC proximity of TMDCs, and Néel-type skyrmions have been observed by Lorentz transmission electron microscopy [9]. However, no experiments have demonstrated the boundary accumulation of magnons yet, which is important for the demonstration of its non-Hermitian bulk-boundary correspondence in magnetic systems.

Here we fabricate monolayer WSe_2/Fe_3GeTe_2 (FGT) vdW heterostructure and analyze its magnetotransport behavior from the bulk and edge. In this heterostructure, strong SOC proximity effect of WSe_2 [26–28] and broken inversion symmetry at the interface would lead to an interfacial DMI and facilitate the observation of NHSE of magnons. Experimentally, we find that the negative magnetoresistance (NMR) in WSe_2/FGT heterostructure at the edge is larger than that at the bulk, revealing stronger electron-magnon scattering at the boundaries, which is consistent with the scenario of magnonic NHSE. The temperature dependence of NMR evolves nonmonotonically below the Curie temperature T_C, which is attributed to the hybrid effect of electron-magnon and electron-magnetic impurity scatterings. Our work sheds light on non-Hermitian physics of magnons in condensed matter.

*anqi0112@pku.edu.cn
†liaozm@pku.edu.cn

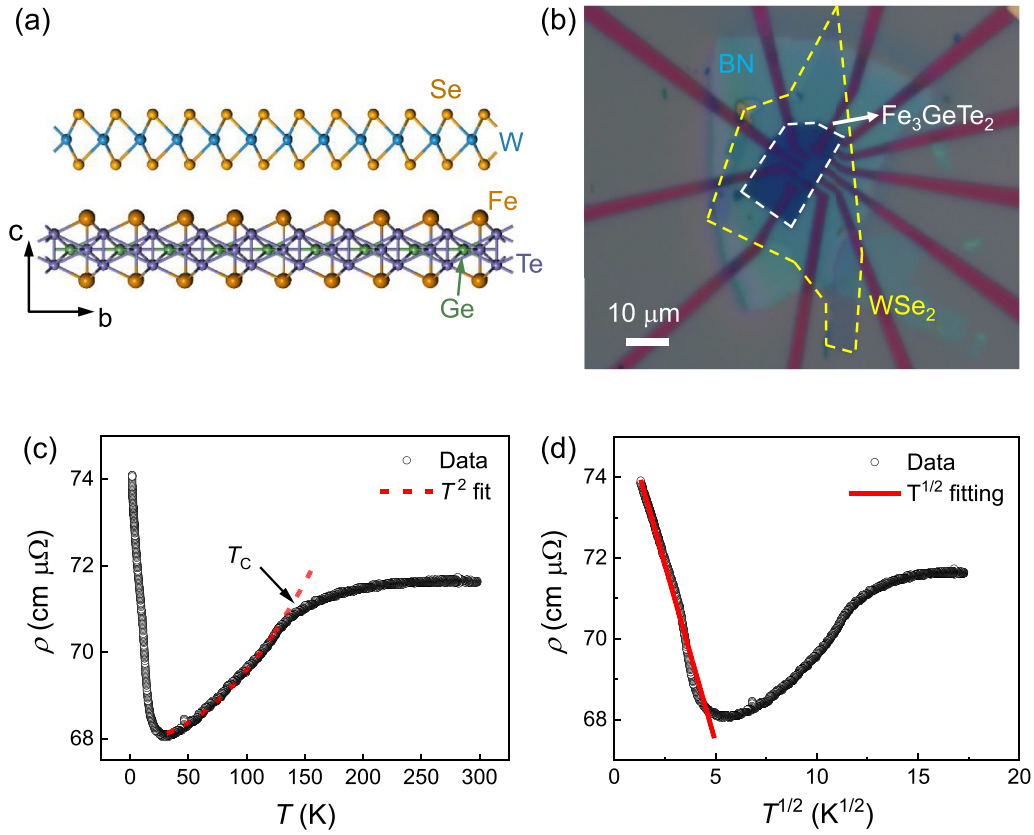

FIG. 1. Characterization of the BN/WSe_2/FGT device. (a) Atomic structure of monolayer WSe_2 (upper panel) and Fe_3GeTe_2 (FGT) (lower panel). The vdW gap between adjacent layers in FGT is 2.95 Å. (b) Optical image of device 2. FGT thin flake and monolayer WSe_2 are outlined by the white and yellow dashed lines, respectively. The device is encapsulated by BN (light blue, ∼20 nm thick) for protection. Ti/Au bottom electrodes (red strips) were prepared before the transfer process. (c) ρ-T curve measured via the standard four-terminal method from 300 to 1.8 K in device 2. Resistivity from 160 to 40 K is fitted by the quadratic temperature dependence (dashed red curve). (d) ρ-T in the $T^{1/2}$ scale. The red line at low temperatures is a guide to the eyes.

II. EXPERIMENTAL METHOD

The WSe_2 and FGT bulk materials were obtained commercially, with their atomic structure shown in Fig. 1(a). Bulk FGT has an interlayer van der Waals gap of 2.95Å, and it has a strong magnetocrystalline anisotropy which induces long-range ferromagnetic order in thin layer FGT. We fabricated Ti(2 nm)/Au(10 nm) bottom electrodes on SiO_2/Si substrates using electron beam lithography (EBL) and electron beam evaporation (EBE), followed by plasma etching to remove polymer residues and dangling bonds. The channel length between the neighboring electrodes is ∼1 μm. Thin flakes were exfoliated mechanically from the bulk materials. The BN/WSe_2/FGT device was fabricated by the "tear and stack" technique and transferred onto the bottom electrodes (see Appendix A). To manifest the edge transport, one long straight edge of the FGT was inserted into the electrodes no longer than 300 nm to eliminate the bulk conduction component. Figure 1(b) shows the optical image of a typical device. Two rows of bottom electrodes featuring different configurations were designed, one for bulk detection and the other for edge measurement. The transport measurements were carried out in an Oxford cryostat equipped with a superconducting magnet and a variable temperature insert with a base temperature of 1.8 K. Standard lock-in techniques were used to measure the transport signals. Reproducible magnetotransport results were obtained from different devices (see Appendix B). Here we mainly report the results of four typical devices, marked as devices 1, 2, 3, and 4.

III. RESULTS AND DISCUSSION

Figure 1(c) exhibits the ρ-T curve measured by the four-terminal method of a monolayer WSe_2/FGT (∼10 nm) device from 300 to 1.8 K. The resistivity decreases as the temperature goes down from 300 to 40 K, showing a typical metallic feature. A kink at ∼160 K reveals the Curie temperature T_C, demonstrating the phase transition of FGT from paramagnetic to ferromagnetic when cooling down. Within the intermediate temperature region from 160 to 40 K, the resistivity exhibits a T^2 dependence, as fitted by the dashed red curve in Fig. 1(c). The quadratic dependence is consistent with the electron-magnon scattering mechanism, with $1/\tau \propto T^2$ below T_C, where τ is the transport relaxation time [29,30]. Below 40 K, a resistivity upturn is observed, and the resistivity approximately follows a $-T^{1/2}$ dependence down to the base temperature [Fig. 1(d)], which is reminiscent of the electron-electron interaction (EEI) for three-dimensional (3D) systems [31]. A recent study also suggests the possible contribution of

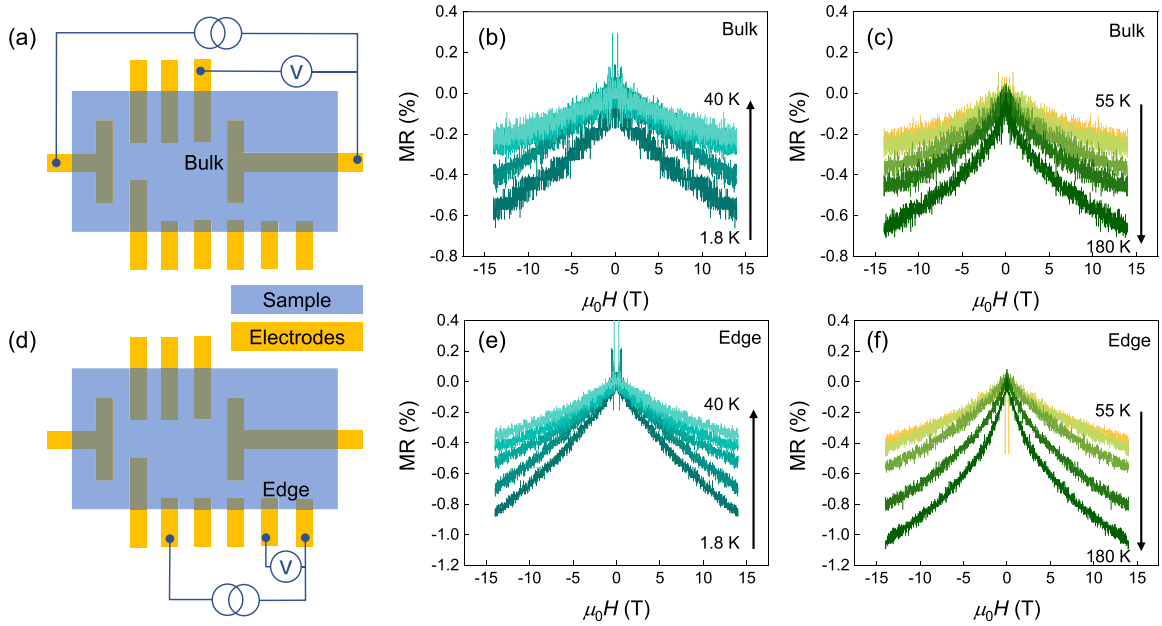

FIG. 2. Negative magnetoresistance measured from device 2. (a) Schematic of the measurement setup for bulk detection. Magnetoresistance (MR) of the bulk at temperatures from 1.8 to 40 K (b) and from 55 to 180 K (c). (d)–(f) Same as (a)–(c) but for the edge detection. All data are symmetrized to remove the transverse components. MR is defined as $[R(\mu_0 H) - R(0)]/R(0) \times 100\%$.

the orbital two-channel Kondo effect to the abrupt resistance increase [32].

The magnetoresistance (MR) of the bulk and the edge at different temperatures is studied. The measurement configuration for the bulk and the edge are shown in Figs. 2(a) and 2(d), respectively. Electrodes are inserted less than 300 nm at one side of the FGT flake for edge detection, and more than 7 μm at the opposite side for bulk detection. We scan the magnetic field from −14 to 14 T and record the resistance signals [Figs. 2(b) and 2(c), Figs. 2(e) and 2(f)]. All data are symmetrized to remove the transverse components, where MR is defined as $[R(\mu_0 H) - R(0)]/R(0) \times 100\%$. We notice that a monotonic and nonsaturating NMR is obtained for both bulk and edge configurations at all temperatures. Various mechanisms could lead to the NMR, e.g., weak localization (WL), electron-magnon scattering, and magnetic impurity scattering. NMR has been observed in Mg films due to WL [33,34], as increasing magnetic field gradually breaks the phase coherence of the time-reversal-symmetric pair of interference loops. However, in a ferromagnetic metal with long-range magnetic order, WL could hardly happen due to the intrinsic broken time-reversal symmetry, which could be ruled out as the origin. Besides, disorders in artificial systems are also likely to cause the NMR effect [35]. Previous studies have suggested that the NMR induced by disorder decreases with increasing temperature [36,37]. While in our work, the NMRs of bulk and edge both show nonmonotonic temperature dependence (Fig. 2). And the disorder scenario cannot explain the stronger NMR at the edge while the local resistivity of edge and bulk is close. Therefore, the disorder scenario can be safely excluded as the main origin of NMR. At finite temperatures, magnons exist as collective modes of excited magnetic states. The electron-magnon scattering would contribute to the transport relaxation time τ, thus increasing the resistivity. NMR follows under an external magnetic field due to the magnetic suppression of magnon populations [38,39]. Though being broadly considered as an itinerant magnet [32,40,41], related spectroscopy studies suggest the dual properties (itinerant and localized) of Fe 3*d* electrons may result in a rather complicated magnetism in FGT [42,43]. Therefore, the spin-dependent scattering off the local magnetic moments may also take place. Under a magnetic field, NMR occurs due to the

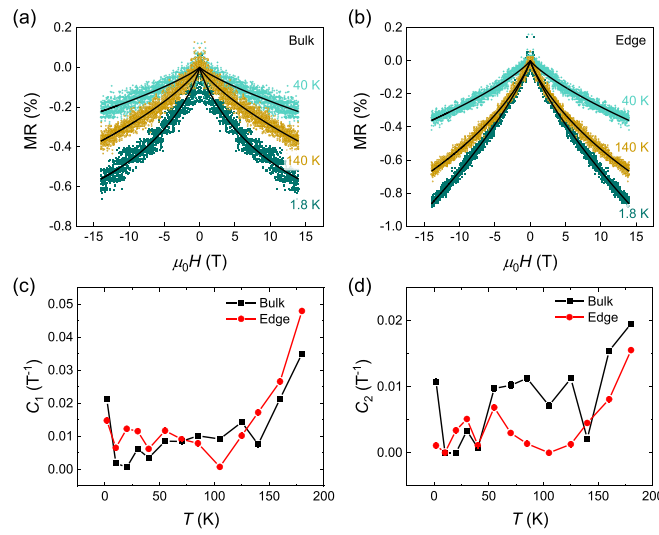

FIG. 3. Modeling the NMR at different temperatures in device 2. The MR is fitted by an electron-magnon scattering model for bulk (a) and edge (b), respectively, as plotted by the black lines. Data at three representative temperatures are shown for clarity. The extracted parameters C_1 (c) and C_2 (d) are plotted for bulk (black symbols) and edge (red symbols), respectively.

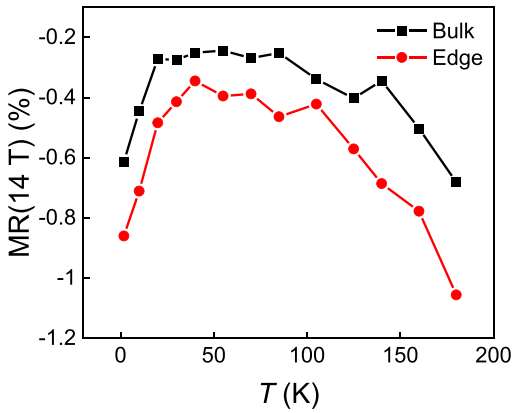

FIG. 4. Enhanced NMR at the edge of device 2. Temperature dependence of MR at 14 T for bulk and edge. Both bulk (black symbols) and edge (red symbols) NMR show a nonmonotonic behavior and reach their minimum (absolute value) at ∼40 K.

alignment of the impurities' moments which enhances the transport relaxation time τ. Thus, the observed NMR is related to the suppression of magnon excitations and the alignment of magnetic impurities.

To quantify the observed NMR in WSe_2/FGT heterojunction, we fit the data with an electron-magnon scattering model proposed by Raquet *et al.* [38]:

$$\mathrm{MR} = C_1 \mu_0 H \ln(C_2 \mu_0 H), \tag{1}$$

where $C_1 \propto T/D(T)^2$, $C_2 = \mu_B/k_B T$, and $D(T)$ is the magnon stiffness. The NMRs of bulk and edge at all temperatures are well fitted by Eq. (1), as depicted by the black lines in Figs. 3(a) and 3(b), where for clarity we only plot data at three temperature points. The extracted C_1 shows an approximately monotonic temperature dependence [Fig. 3(c)]. To the lowest order approximation, $D(T) \approx D_0 - D_1 T^2$, thus resulting in an increasing $T/D(T)^2$ with T, consistent with our observations. Figure 3(d) plots the fitted C_2 for bulk and edge. The temperature evolution deviates from the model's expectations ($\propto 1/T$), suggesting an additional mechanism resulting in NMR besides electron-magnon scattering. Considering the likely localized property of Fe $3d$ electrons in FGT [42,43], we adopt a semiempirical MR expression based on localized magnetic moments derived by Khosla and Fischer [44]. Interestingly, the NMR could also be well fitted (see Fig. 6 and Appendix C for details). Therefore, the NMR in FGT could be a combined action of the two aforementioned origins.

From Figs. 2 and 3, we see that both the bulk and the edge NMR manifest nonmonotonic temperature dependence, as recognized more clearly in Fig. 4. The NMR amplitude (absolute value) reaches its minimum at ∼40 K. Interestingly, this temperature corresponds to the transition point of resistivity upturn [Fig. 1(c)]. The stronger NMR effect at the higher temperature regime could be well understood within the electron-magnon scattering scenario, since more magnons are excited with increasing thermal fluctuation. When applying a magnetic field, the damped spin waves cause a considerable decrease in resistance. As further increasing the temperature beyond the FGT Curie temperature T_C, magnon excitations are gradually diminished, and electron-magnetic impurity scattering comes into prominence. As shown in Fig. 7, the NMR persists up to 240 K, far above T_C, which could be well fitted by the electron-localized moments scattering model (see Appendix D). For $T < 40$ K, the enhanced NMR at low temperatures seems puzzling, considering magnons are suppressed exponentially when cooling down [45]. We suppose that this enhancement may result from the variation in magnetic impurities at low temperatures and the effect of EEI. Similar results have been observed previously, where the authors relate this anomalous increase to the orbital two-channel Kondo effect [32].

A notable feature is that the NMR of the edge is larger than that of the bulk at all temperatures (Fig. 4). Below we discuss the possible origins of the edge-enhanced NMR in WSe_2/FGT heterostructure. First, we notice that the normalized remanence and coercive field at bulk and edge are almost identical (see Fig. 8 and Appendix E), revealing uniform magnetism in the sample plane. Thus, the spin-related scatterings with local magnetic moments could hardly cause such a distinction in NMR between bulk and edge. The edge-enhanced NMR most possibly stems from the aggregation of bulk magnons toward the boundaries, resulting in stronger electron-magnon scatterings at the sample's edges. Usually, magnons distribute uniformly in a ferromagnet. The edge enhancement here arises from the proximity coupling between WSe_2 and FGT. At the interface, with broken inversion symmetry, the Rashba SOC of WSe_2 could cause a DMI in the heterostructure [9]. Recent theories predict that the magnon skin effect exists in magnetic systems with strong DMI and magnetic dissipations [18,46]. The dissipative interactions may take place in WSe_2/FGT due to magnon-electron, magnon-phonon interactions, and magnon scattering on impurity moments, which act as an effective non-Hermitian term in lattice Hamiltonian. The resulting complex energy spectrum gains a finite effective spectrum area with appropriate thermal excitations below T_C, and the NHSE follows [14,18,47]. As a result, stronger electron-magnon scatterings at the boundaries lead to an edge-enhanced NMR, consistent with the observations. Our experimental results provide evidence for the magnonic NHSE in magnetic systems with DMI and dissipation.

IV. CONCLUSIONS

In summary, the edge-enhanced NMR in monolayer WSe_2/FGT heterostructure is observed, indicating the aggregation of bulk magnons towards the boundaries. The temperature evolution of NMR exhibits a nonmonotonic dependence, which is attributed to the coexistence of electron-magnon scattering and magnetic impurity scattering. The results serve as signatures for NHSE of magnons, which originate from the magnetic dissipation and the DMI induced by WSe_2 with strong SOC. Next-step experiments with a high spatial resolution like Brillouin scattering are required to demonstrate the distribution of magnons at bulk and edge more directly. Our work sheds light on non-Hermitian bulk-boundary correspondence in a vdW ferromagnet with DMI, paving the way for further study in exceptional topology in quantum materials.

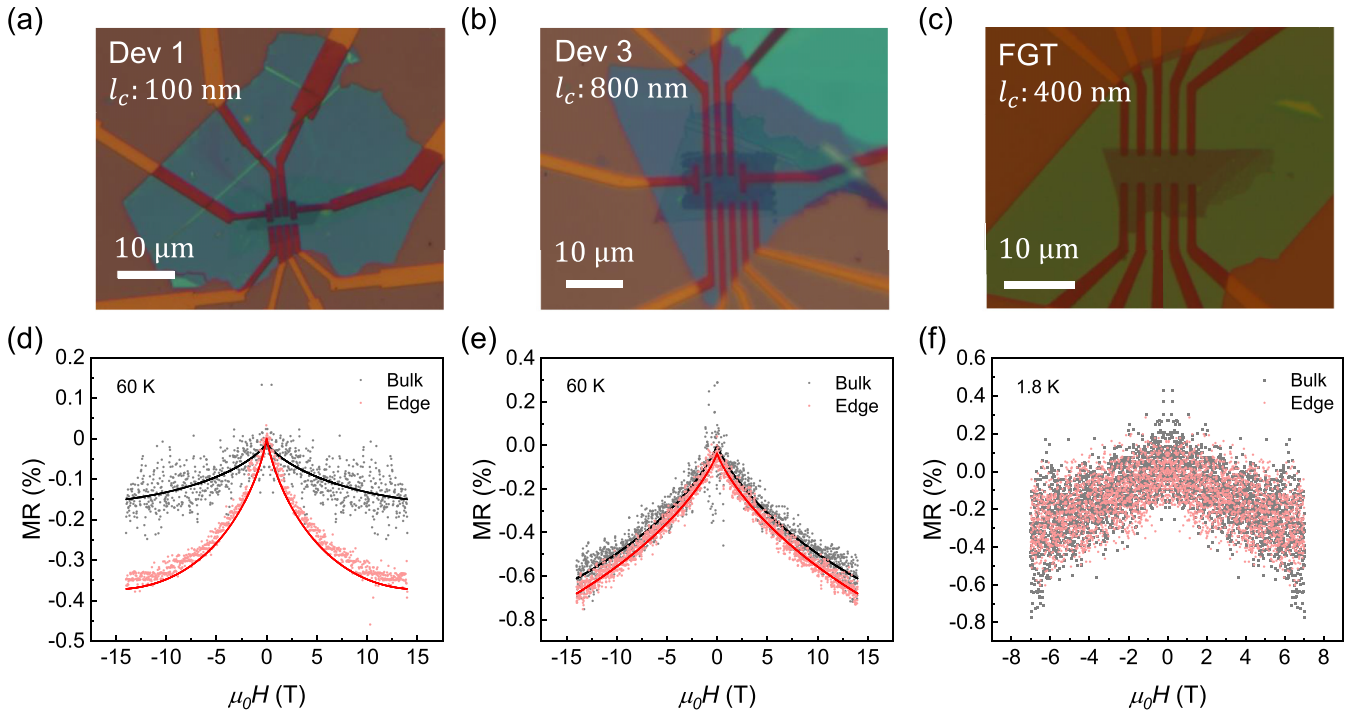

FIG. 5. NMR effect of other two FGT/WSe_2 devices (a),(b) and FGT alone (c).

ACKNOWLEDGMENTS

This work was supported by the Key-Area Research and Development Program of Guangdong Province (Grant No. 2020B0303060001), National Natural Science Foundation of China (Grants No. 91964201, No. 61825401, and No. 12204016), China Postdoctoral Science Foundation (Grant No. 2021M700254), and the Innovation Program for Quantum Science and Technology (Grant No. 2021ZD0302403).

APPENDIX A: DEVICE FABRICATION VIA TEAR AND STACK METHOD

All the van der Waals (vdW) materials were exfoliated mechanically from the bulk materials. In more details, the thick film was first dissociated through transparent tape, and further thinned by PDMS. The thin film was then transferred onto Si/SiO_2 substrate by heating at 100 °C for 1 min. The Fe_3GeTe_2 thin flakes with long straight edges were selected to construct the devices. Next, BN flake, monolayer WSe_2 and few-layer FGT were sequentially picked up and then transferred onto the Ti/Au electrodes using a polymer-based dry transfer technique. The whole processes were done in an argon-filled glove box to avoid sample degradation. Finally, the device was soaked in chloroform to remove the polymer on top of the device and finally rinsed thoroughly with acetone.

APPENDIX B: NEGATIVE MAGNETORESISTANCE OBSERVED IN DIFFERENT DEVICES

The difference of NMR between the edge and bulk is widely observed in our devices. Figures 5(a) and 5(b) show the other two WSe_2/FGT devices with similar electrode structure, but the edge electrodes have different edge contact length (l_c) with the FGT layer. As $l_c < 500$ nm, the NMR at the edge is much larger than that in bulk, consistent with the results in the main text. As $l_c > 500$ nm, there is little difference observed, which may be related to the increased bulk contribution in the edge measurements. Figure 5(c) shows a pure FGT device without WSe_2, where the bulk and edge show a similar NMR effect as expected [Fig. 5(f)]. All the three devices were measured by the four-terminal method at edge and bulk.

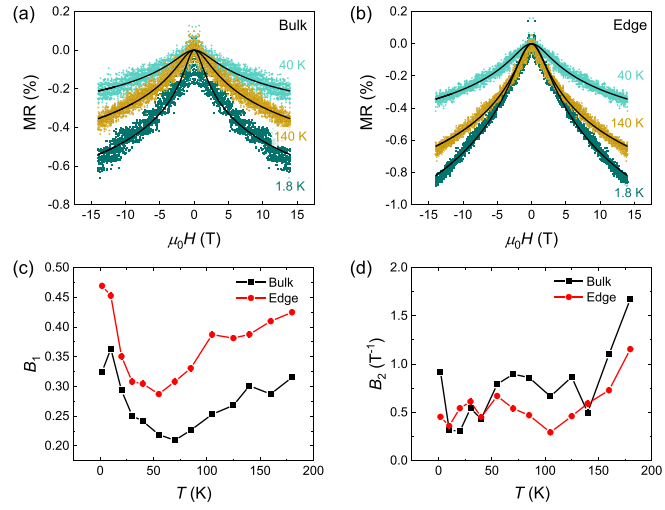

FIG. 6. Analysis of temperature-dependent NMR via electron-magnetic impurity scattering model in device 2. The MR is fitted by a localized magnetic moments model for bulk (a) and edge (b) measurement, respectively, as plotted by the black lines. Data at three representative temperatures are shown for clarity. The extracted parameters B_1 (c) and B_2 (d) are plotted for bulk (black symbols) and edge (red symbols), respectively.

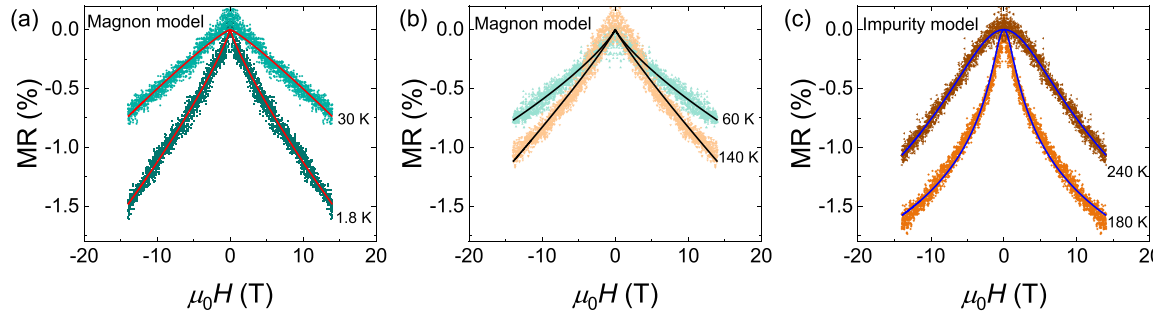

FIG. 7. Temperature-dependent MR results measured at the edge of device 4. Robust NMR is observed up to 240 K, far above the Curie temperature (∼160 K), which could be well fitted by the electron-magnetic impurity moments scattering model.

APPENDIX C: NMR FITTED WITH A LOCALIZED MAGNETIC MOMENTS MODEL

Considering the Fe 3*d* orbitals may exhibit localized properties, we also fit the NMR in the electron-localized moments scattering scenario [44]:

$$\mathrm{MR} = -B_1^2 \ln\left(1 + B_2^2 \mu_0^2 H^2\right). \tag{C1}$$

The fitting results are shown as black lines in Figs. 6(a) and 6(b) for bulk and edge, respectively. The extracted parameters B_1 and B_2 of Eq. (C1) both show nonmonotonic temperature dependence [Figs. 6(c) and 6(d)].

APPENDIX D: NEGATIVE MAGNETORESISTANCE OBSERVED ABOVE THE FGT CURIE TEMPERATURE

Figure 7 shows the MR data of device 4 from 1.8 to 240 K, which is far above the FGT Curie temperature T_C (∼160 K). Below T_C, the NMR can be understood by considering both the electron-magnon and electron-magnetic impurity scatterings. Similar to device 2, both scattering models can well fit the MR data. Figures 7(a) and 7(b) demonstrate the fitting results by the electron-magnon scattering model. Upon increasing the temperature towards and above T_C, magnon excitations are gradually diminished, and the magnetic impurity scattering mechanism dominates. As shown in Fig. 7(c), the NMR is still observable up to 240 K, far above T_C,

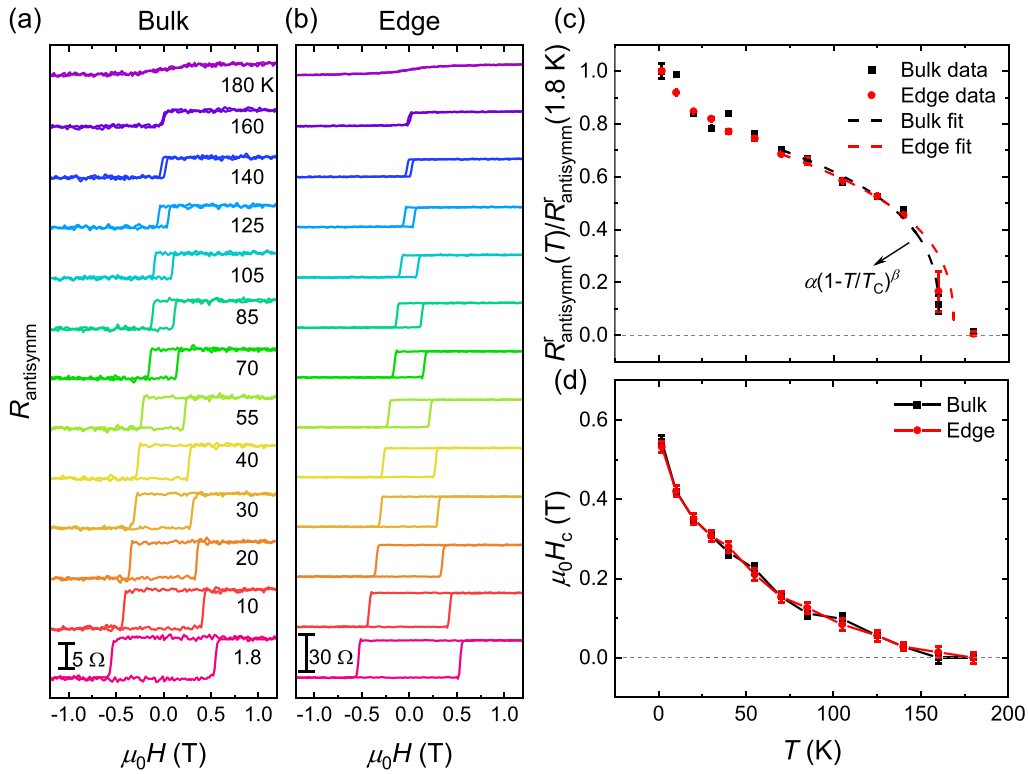

FIG. 8. Magnetic hysteresis obtained at the bulk and edge of device 2. Bulk (a) and edge (b) transverse resistance hysteresis loops at temperatures from 1.8 to 180 K. Signals are antisymmetrized to remove the longitudinal components. Normalized remanence (c) and coercivity (d) at bulk (black symbols) and edge (red symbols) versus temperature extracted from (a) and (b). The dashed lines in (c) are the criticality fits $\alpha(1-T/TC)^\beta$ near the Curie temperature T_C. The obtained critical exponent β is 0.31 and 0.34 for bulk and edge remanence, respectively.

which could be well fitted by the electron-localized moments scattering model. Notably, either electron-magnon scattering or magnetic impurity scattering cannot solely produce the spatially and temperature dependent NMR observed in our work. Only the electron-magnetic impurity scattering cannot explain the edge-enhanced NMR. Only the electron-magnon scatterings cannot elucidate the NMR far above the Curie temperature of FGT. It is worthwhile to note that the NMR increases as temperature increases from 60 to 140 K [Fig. 7(b)]. This is consistent with the fact that increasing the temperature will increase the excitation of magnons. Further increasing temperature above T_C from 180 to 240 K, the NMR is reduced. This is because an increase in temperature will cause an increase in phonon scattering, while the contribution of magnetic impurity scattering to the total resistance decreases.

APPENDIX E: ANTISYMMETRIZED RESISTANCE AT BULK AND EDGE

Due to the slight misalignment of the electrodes, the resistance signals contain both the transverse and longitudinal components. We extract the transverse signals R_{antisymm} by antisymmetrizing the measured resistance at various temperatures, as shown in Figs. 8(a) and 8(b) for the bulk and the edge, respectively. For both bulk and edge, the magnetic hysteresis forms a rectangular loop with the coercive field being $\sim \pm 0.55$ T at 1.8 K, which gradually shrinks as increasing temperatures and disappears at ~180 K. The sharp rectangular loop reflects the strong perpendicular magnetic anisotropy (PMA) of FGT. Despite the difference in the absolute value, the normalized remanence of the bulk and the edge follows a similar temperature dependence [Fig. 8(c)]; so does the coercive field $\mu_0 H_c$ [Fig. 8(d)]. The nearly identical behavior of the bulk and edge suggests the homogeneity of magnetism in the WSe_2/FGT heterostructure. The criticality fit $\alpha(1-T/TC)^{\beta}$ is performed near the T_C [dashed lines in Fig. 8(c)]. The obtained critical exponent β is 0.31 and 0.34 for bulk and edge configurations, respectively, in good agreement with the theoretical prediction of 0.33 in the 3D Ising model due to its quasi-3D nature (thickness of FGT ~10 nm). The absence of intermediate magnetic states within the hysteresis loops [40] suggests that the FGT thin flake is likely of a single domain. With an increasing magnetic field, the domain walls are forced to a uniform state and form a full magnetization beyond the coercive field.

[1] I. Dzyaloshinsky, A thermodynamic theory of "weak" ferromagnetism of antiferromagnetics, J. Phys. Chem. Solids **4**, 241 (1958).

[2] T. Moriya, Anisotropic superexchange interaction and weak ferromagnetism, Phys. Rev. **120**, 91 (1960).

[3] S. Woo, K. Litzius, B. Krueger, M.-Y. Im, L. Caretta, K. Richter, M. Mann, A. Krone, R. M. Reeve, M. Weigand *et al.*, Observation of room-temperature magnetic skyrmions and their current-driven dynamics in ultrathin metallic ferromagnets, Nat. Mater. **15**, 501 (2016).

[4] C. Moreau-Luchaire, C. Moutafis, N. Reyren, J. Sampaio, C. A. F. Vaz, N. Van Horne, K. Bouzehouane, K. Garcia, C. Deranlot, P. Warnicke *et al.*, Additive interfacial chiral interaction in multilayers for stabilization of small individual skyrmions at room temperature, Nat. Nanotechnol. **11**, 444 (2016).

[5] O. Boulle, J. Vogel, H. Yang, S. Pizzini, D. d. S. Chaves, A. Locatelli, T. O. Mentes, A. Sala, L. D. Buda-Prejbeanu, O. Klein *et al.*, Room-temperature chiral magnetic skyrmions in ultrathin magnetic nanostructures, Nat. Nanotechnol. **11**, 449 (2016).

[6] J. Sampaio, V. Cros, S. Rohart, A. Thiaville, and A. Fert, Nucleation, stability and current-induced motion of isolated magnetic skyrmions in nanostructures, Nat. Nanotechnol. **8**, 839 (2013).

[7] S. Heinze, K. von Bergmann, M. Menzel, J. Brede, A. Kubetzka, R. Wiesendanger, G. Bihlmayer, and S. Bluegel, Spontaneous atomic-scale magnetic skyrmion lattice in two dimensions, Nat. Phys. **7**, 713 (2011).

[8] H. Yang, G. Chen, A. A. C. Cotta, A. T. N'Diaye, S. A. Nikolaev, E. A. Soares, W. A. A. Macedo, K. Liu, A. K. Schmid, A. Fert *et al.*, Significant Dzyaloshinskii–Moriya interaction at graphene–ferromagnet interfaces due to the Rashba effect, Nat. Mater. **17**, 605 (2018).

[9] Y. Wu, S. Zhang, J. Zhang, W. Wang, Y. L. Zhu, J. Hu, G. Yin, K. Wong, C. Fang, C. Wan *et al.*, Néel-type skyrmion in WTe_2/Fe_3GeTe_2 van der Waals heterostructure, Nat. Commun. **11**, 3860 (2020).

[10] R. Tomasello, E. Martinez, R. Zivieri, L. Torres, M. Carpentieri, and G. Finocchio, A strategy for the design of skyrmion racetrack memories, Sci. Rep. **4**, 6784 (2014).

[11] S. S. P. Parkin, M. Hayashi, and L. Thomas, Magnetic domain-wall racetrack memory, Science **320**, 190 (2008).

[12] A. Fert, N. Reyren, and V. Cros, Magnetic skyrmions: Advances in physics and potential applications, Nat. Rev. Mater. **2**, 17031 (2017).

[13] E. J. Bergholtz, J. C. Budich, and F. K. Kunst, Exceptional topology of non-hermitian systems, Rev. Mod. Phys. **93**, 015005 (2021).

[14] S. Yao and Z. Wang, Edge states and topological invariants of non-Hermitian systems, Phys. Rev. Lett. **121**, 086803 (2018).

[15] S. Yao, F. Song, and Z. Wang, Non-Hermitian Chern Bands, Phys. Rev. Lett. **121**, 136802 (2018).

[16] H. Shen, B. Zhen, and L. Fu, Topological band theory for non-Hermitian Hamiltonians, Phys. Rev. Lett. **120**, 146402 (2018).

[17] Z. Gong, Y. Ashida, K. Kawabata, K. Takasan, S. Higashikawa, and M. Ueda, Topological phases of non-Hermitian systems, Phys. Rev. X **8**, 031079 (2018).

[18] K. Deng and B. Flebus, Non-Hermitian skin effect in magnetic systems, Phys. Rev. B **105**, L180406 (2022).

[19] A. Galda and V. M. Vinokur, Parity-time symmetry breaking in magnetic systems, Phys. Rev. B **94**, 020408(R) (2016).

[20] P. A. McClarty and J. G. Rau, Non-Hermitian topology of spontaneous magnon decay, Phys. Rev. B **100**, 100405(R) (2019).

[21] A. Galda and V. M. Vinokur, Exceptional points in classical spin dynamics, Sci. Rep. **9**, 17484 (2019).
[22] Y. Tserkovnyak, Exceptional points in dissipatively coupled spin dynamics, Phys. Rev. Res. **2**, 013031 (2020).
[23] H. Liu, D. Sun, C. Zhang, M. Groesbeck, R. McLaughlin, and Z. V. Vardeny, Observation of exceptional points in magnonic parity-time symmetry devices, Sci. Adv. **5**, eaax9144 (2019).
[24] D. Zhang, X.-Q. Luo, Y.-P. Wang, T.-F. Li, and J. Q. You, Observation of the exceptional point in cavity magnon-polaritons, Nat. Commun. **8**, 1368 (2017).
[25] X. Zhang, K. Ding, X. Zhou, J. Xu, and D. Jin, Experimental observation of an exceptional surface in synthetic dimensions with magnon polaritons, Phys. Rev. Lett. **123**, 237202 (2019).
[26] G.-B. Liu, W.-Y. Shan, Y. Yao, W. Yao, and D. Xiao, Three-band tight-binding model for monolayers of group-VIB transition metal dichalcogenides, Phys. Rev. B **88**, 085433 (2013).
[27] B. Yang, E. Molina, J. Kim *et al.*, Effect of distance on photoluminescence quenching and proximity-induced spin–orbit coupling in graphene/WSe_2 heterostructures, Nano Lett. **18**, 3580 (2018).
[28] B. Fülöp, A. Márffy, S. Zihlmann *et al.*, Boosting proximity spin–orbit coupling in graphene/WSe_2 heterostructures via hydrostatic pressure, NPJ 2D Mater. Appl. **5**, 82 (2021).
[29] R. G. Chambers, *Electronics in Metals and Semiconductors* (Springer Netherlands, Dordrecht, 1990).
[30] P. D. Desai, H. M. James, and C. Y. Ho, Electrical resistivity of aluminum and manganese, J. Phys. Chem. Ref. Data **13**, 1131 (1984).
[31] P. A. Lee and T. V. Ramakrishnan, Disordered electronic systems, Rev. Mod. Phys. **57**, 287 (1985).
[32] H. Feng, Y. Li, Y. Shi, H.-Y. Xie, Y. Li, and Y. Xu, Resistance anomaly and linear magnetoresistance in thin flakes of itinerant ferromagnet Fe_3GeTe_2, Chin. Phys. Lett. **39**, 077501 (2022).
[33] G. Bergmann, Measurement of the magnetic scattering time by weak localization, Phys. Rev. Lett. **49**, 162 (1982).
[34] G. Bergmann, Quantitative analysis of weak localization in thin Mg films by magnetoresistance measurements, Phys. Rev. B **25**, 2937 (1982).
[35] Y.-B. Zhou, B.-H. Han, Z.-M. Liao, H.-C. Wu, and D.-P. Yu, From positive to negative magnetoresistance in graphene with increasing disorder, Appl. Phys. Lett. **98**, 222502 (2011).
[36] T. Iwasaki, S. Nakamura, O. G. Agbonlahor, M. Muruganathan, M. Akabori, Y. Morita, S. Moriyama, S. Ogawa, Y. Wakayama, H. Mizuta, and S. Nakaharai, Room-temperature negative magnetoresistance of helium-ionirradiated defective graphene in the strong Anderson localization regime, Carbon **175**, 87 (2021).
[37] X. Zhang, Q. Z. Xue, and D. D. Zhu, Positive and negative linear magnetoresistance of graphite, Phys. Lett. A **320**, 471 (2004).
[38] B. Raquet, M. Viret, E. Sondergard, O. Cespedes, and R. Mamy, Electron-magnon scattering and magnetic resistivity in 3*d* ferromagnets, Phys. Rev. B **66**, 024433 (2002).
[39] J. G. Checkelsky, M. Lee, E. Morosan, R. J. Cava, and N. P. Ong, Anomalous Hall effect and magnetoresistance in the layered ferromagnet $Fe_{1/4}TaS_2$: The inelastic regime, Phys. Rev. B **77**, 014433 (2008).
[40] Z. Fei, B. Huang, P. Malinowski, W. Wang, T. Song, J. Sanchez, W. Yao, D. Xiao, X. Zhu, A. F. May *et al.*, Two-dimensional itinerant ferromagnetism in atomically thin Fe_3GeTe_2, Nat. Mater. **17**, 778 (2018).
[41] Y. Deng, Y. Yu, Y. Song, J. Zhang, N. Z. Wang, Z. Sun, Y. Yi, Y. Z. Wu, S. Wu, J. Zhu *et al.*, Gate-tunable room-temperature ferromagnetism in two-dimensional Fe_3GeTe_2, Nature (London) **563**, 94 (2018).
[42] Y. Zhang, H. Lu, X. Zhu, S. Tan, W. Feng, Q. Liu, W. Zhang, Q. Chen, Y. Liu, X. Luo *et al.*, Emergence of Kondo lattice behavior in a van der Waals itinerant ferromagnet, Fe_3GeTe_2, Sci. Adv. **4**, eaao6791 (2018).
[43] X. Xu, Y. W. Li, S. R. Duan, S. L. Zhang, Y. J. Chen, L. Kang, A. J. Liang, C. Chen, W. Xia, Y. Xu *et al.*, Signature for non-Stoner ferromagnetism in the van der Waals ferromagnet Fe_3GeTe_2, Phys. Rev. B **101**, 201104(R) (2020).
[44] R. P. Khosla and J. R. Fischer, Magnetoresistance in degenerate CdS: Localized magnetic moments, Phys. Rev. B **2**, 4084 (1970).
[45] W. Gil, D. Görlitz, M. Horisberger, and J. Kötzler, Magnetoresistance anisotropy of polycrystalline cobalt films: Geometrical-size and domain effects, Phys. Rev. B **72**, 134401 (2005).
[46] H. M. Hurst and B. Flebus, Non-hermitian physics in magnetic systems, J. Appl. Phys. **132**, 220902 (2022).
[47] K. Zhang, Z. Yang, and C. Fang, Universal non-Hermitian skin effect in two and higher dimensions, Nat. Commun. **13**, 2496 (2022).